DOI: 10.13009/EUCASS2025-227
11TH EUROPEAN CONFERENCE FOR AERONAUTICS AND SPACE SCIENCES (EUCASS)

Implementation and verification of a shock-fitting technique coupled with the SU2 code

Valerio Orlandini[⋆†], *Renato Paciorri*[⋆] *and Aldo Bonfiglioli*[b]
[⋆]*University of Rome La Sapienza*
Via Eudossiana, 18, 00184, Rome, Italy
[b]*University of Basilicata*
Via dell'Ateneo Lucano 10, 85100, Potenza, Italy
valerio.orlandini@uniroma1.it · renato.paciorri@uniroma1.it · aldo.bonfiglioli@unibas.it
[†]Corresponding author

Abstract

A shock-fitting methodology for unstructured grids is implemented and verified within the open−source CFD solver SU2. The approach accurately tracks shock surfaces as zero-thickness discontinuities embedded in the computational mesh, eliminating numerical diffusion typically present in shock-capturing methods. The technique is validated through a series of test cases, including inviscid and viscous hypersonic flows, as well as fluid-structure interaction (FSI) simulations involving deformable membranes. Comparisons with analytical solutions and reference data demonstrate improved accuracy, convergence, and robustness compared to traditional shock-capturing approaches.

1. Introduction

Numerical simulation of hypersonic flows around blunt bodies using shock-capturing (S-C) solvers continues to present several critical challenges, sometimes resulting in unexpected and undesirable results. Among the most significant problems are stagnation point anomalies,[13] spurious numerical oscillations,[7] the carbuncle phenomenon,[24] and a global reduction in solution accuracy downstream of a captured shock.[6] A frequently cited reason, especially in the context of unstructured tetrahedral meshes, is the lack of a truly multidimensional shock-capturing scheme capable of making the numerical solution insensitive to the orientation of the control volume faces with respect to the shock front.[14] Truly multidimensional upwind schemes,[15] and new approaches such as residual distribution or fluctuation splitting methods[10] have been developed for this purpose. However, even these advanced schemes produce carbuncle type instabilities,[3] resulting in a loss of solution accuracy. This behavior is more plausibly related to the numerical nature of shock-capturing, where at least one grid point typically falls within the discontinuity. When instead the shock is made to coincide exactly with a cell interface, feasible in one-dimensional problems via shock-fitting (S-F) or front-tracking methods, the design accuracy of the scheme can be recovered downstream.[8]

Given the difficulty of obtaining a completely mesh-independent solution method, an alternative is to locally align the control volume faces with the shock front. This is achievable in structured meshes and generally produces accurate results, provided that the flow has a single dominant shock, such as a bow shock.[7] However, the presence of multiple shocks and their interactions impose severe limitations on mesh fitting or refinement in structured meshes due to their intrinsic topological constraints, while unstructured meshes overcome these topological limitations. Shock-capturing simulations on unstructured tetrahedral meshes, however, often suffer from poor solution quality near stagnation regions.[9]

An alternative strategy is to apply shock-fitting techniques in unstructured mesh environments. The shock-fitting method involves precisely locating the shock and tracking its motion using Rankine-Hugoniot relations, thus avoiding the inherent numerical diffusion of shock-capturing methods. Originally introduced by Emmons[12] and later popularized by Moretti and co-workers[17,18] in the context of structured meshes, shock-fitting has been widely applied to two and three-dimensional problems.[25]

Recently, however, Paciorri and Bonfiglioli[21] proposed a shock-fitting technique for unstructured two and three-dimensional meshes (UnDiFi), obtaining promising results in the computation of flows with strong shocks and complex shock-shock interactions.[16,22] This technique produces high-quality results[21] and appears to solve many, if not most, of the problems that affect shock-capturing unstructured CFD solvers when used to simulate flows characterized by strong shocks.

DOI: 10.13009/EUCASS2025-227

This technique, recently extended by Orlandini et al.[19,20] also to fluid-structure interaction (FSI) problems involving deformable walls immersed in hypersonic flows, offers a significant advantage in terms of versatility. The shock-fitting algorithm is designed to operate in a loosely coupled framework, enabling it to interact externally with both fluid and structural solvers. In the original work by Paciorri and Bonfiglioli,[21] the flow field was computed using the EulFS solver,[4] an in-house code based on the Fluctuation Splitting approach, whereas in the present study the same shock-fitting methodology has been applied replacing EulFS with SU2,[11] which uses upwind Finite Volume schemes. This modularity makes the approach highly flexible and easily adaptable to different numerical environments and coupling strategies. For example, in the FSI approach described here, implicit non-linear methods are used in the steady case, whereas explicit non-linear are used for unsteady simulations.
In this work, the verification and validation of the technique is presented for four test cases: Eulerian flow on a hemisphere, viscous flow on a sphere, steady and unsteady FSI on a membrane.

2. Computational methods

In the shock-fitting algorithm, shocks are represented as true surface discontinuities. The shock front is modeled as a double-sided zero-thickness triangulated surface that moves through a background tetrahedral mesh covering the entire computational domain, according to the Rankine-Hugoniot jump conditions. At each time step, a local constrained Delaunay tetrahedralization is performed near the shock front to ensure that its triangles are integrated into the surrounding tetrahedral mesh. This fitted shock surface serves as an internal boundary for the SU2 shock-capturing solver used to numerically solve the governing equations within the smooth-flow regions of the flow domain.

2.1 SU2 shock-capturing solver

SU2[11] is a computational analysis and design package that has been developed to solve multiphysics analysis and optimization tasks using unstructured mesh topologies. In the case of compressible flow or high-speed aerodynamics in which high-resolution linear schemes often result in numerical oscillations near the shock, SU2 uses slope limiters to avoid oscillations by damping second-order terms near shocks and other regions with sharp gradients. In this work, we have used the second-order upwind HLLC scheme with Venkatakrishnan's slope limiter[27].

2.2 Unstructured Discontinuity Fitting Algorithm

In this subsection we describe the five algorithmic steps required to advance the solution over a single time step of size Δt:

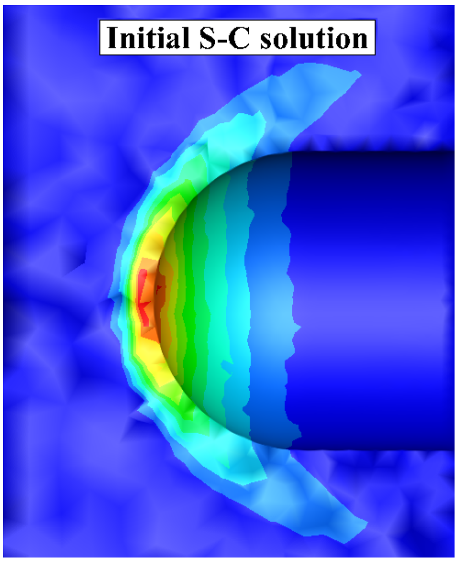

Figure 1: Initial S-C solution

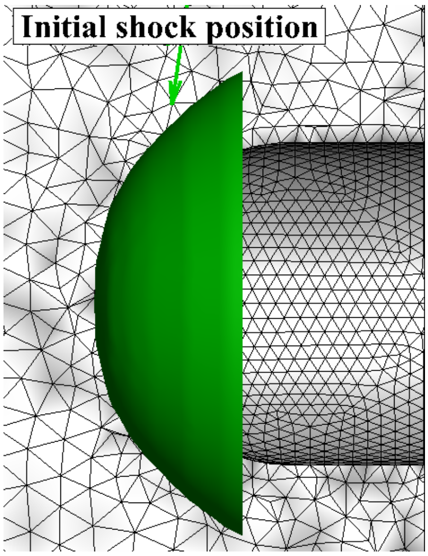

Figure 2: Initial shock position

- Step 0. To initialize the S-F method, it is essential to determine the initial position of the shock wave. This is achieved by first performing an S-C simulation. An initial background grid is generated to obtain the solution

DOI: 10.13009/EUCASS2025-227

depicted in Fig. 1, which illustrates the pressure field around a hemisphere immersed in a hypersonic flow. From the S-C solution, the shock surface - highlighted in green in Fig. 2 - is extracted and subsequently tessellated into triangular elements. In this work, both the volumetric and surface meshes were generated using the ANSA software[1].

- Step 1. The S-F algorithm begins by embedding the triangulated shock surface into the background mesh. This process involves removing all tetrahedral cells intersected by the shock wave and carving out cavities in the affected regions of the mesh. To ensure accurate regeneration of the grid near the discontinuity, nodes located too close to the shock surface are temporarily deactivated - referred to as *ghost points*. These ghost points are excluded from the remeshing process to prevent mesh distortion. The mesh generator TetGen[26] is then employed to fill the cavities using a constrained Delaunay tetrahedralization, ensuring conformity to the shock surface triangulation. Unlike the background mesh, which does not incorporate the fitted discontinuity, the resulting mesh - now containing the triangulated shock surface - is referred to as the *computational mesh*. Fig. 3 illustrates the initial computational mesh produced following shock wave insertion via TetGen.

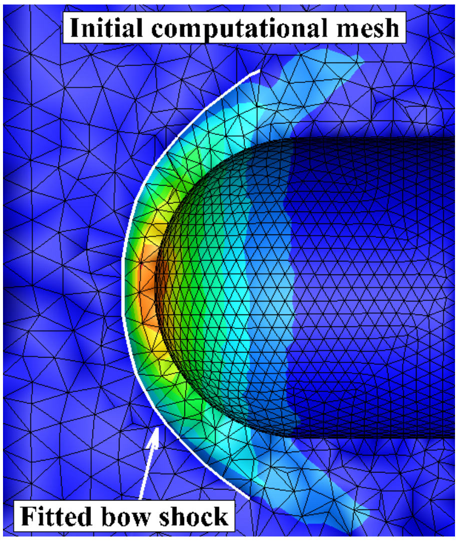

Figure 3: Initial computational mesh

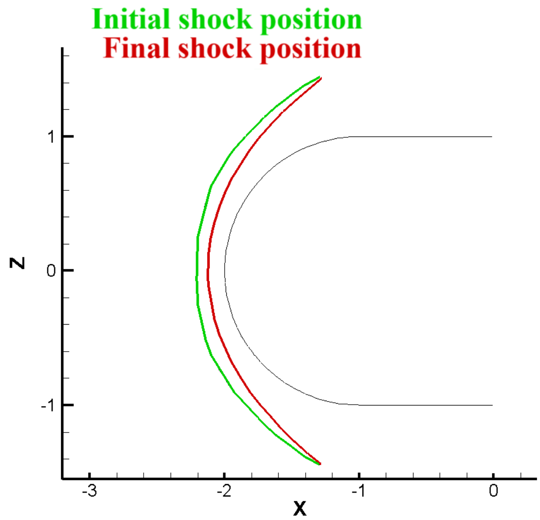

Figure 4: Shock wave displacement

- Step 2. As previously said, the fitted shock surface is considered as an internal boundary for the SU2 shock-capturing solver that updates at time level $t + \Delta t$ the nodal values across the entire grid, including the shock points on both sides of the triangulated discontinuity.

- Step 3. Each shock point is characterized not only by its upstream and downstream flow states, but also by its shock speed, which is aligned with the local shock normal vector $\mathbf{n}$ and has magnitude w. At time level $t + \Delta t$, the shock-upstream state has been updated by the SU2 solver in Step 2. On the downstream side of the shock-surface, however, only the characteristic quantities conveyed towards the shock from its downstream side are available. Therefore, to determine the full downstream state and the shock speed w, the classical Rankine-Hugoniot equations are solved using the Newton-Raphson method. Convergence is typically achieved within a few iterations, with machine precision accuracy. Once the shock speed w is known, the new position of each shock node at time $t + \Delta t$ is computed using the following integration formula:

$$\mathbf{x}_P^{t+\Delta t} = \mathbf{x}_P^t + w^{t+\Delta t}\mathbf{n}\Delta t \tag{1}$$

  Although Eq. (1) is only first-order accurate in time, it does not compromise the overall accuracy of the steady-state solution, which primarily depends on the spatial accuracy of the flow solver and the shock normal estimation. Figure 4 shows the difference between the initial shock position and the final shock position obtained when the steady-state is reached.

- Step 4. The ghost nodes in the background mesh, which were excluded from the computation in Step 1, are not updated by the S-C solver. However, it is essential to update these nodes at time $t + \Delta t$, as the shock front

DOI: 10.13009/EUCASS2025-227

may subsequently move far enough from its current location to require reactivating some of the ghost nodes in the computational domain. This update is performed by first identifying the cell of the computational mesh that contains each ghost node, followed by interpolating its state based on the values at the vertices of the enclosing tetrahedral cell.

Finally, the cycle returns to Step 1 and continues iteratively until convergence is achieved - that is, when the shock speed w approaches zero at all shock-points.

3. Gasdynamic test-cases

To demonstrate the capabilities of the shock-fitting algorithm presented in this work, two test cases are considered. The first involves an inviscid hypersonic Eulerian flow over a hemisphere, while the second focuses on a viscous hypersonic laminar flow over a sphere. Both cases are used to assess the accuracy and robustness of the proposed method through grid convergence analyzes.
In the Eulerian flow over the hemisphere the grid convergence study is performed using only two grid levels, as key reference quantities are known in this case. Specifically, the stagnation pressure and the conservation of the total temperature are used to validate the numerical results against theoretical expectations.
For viscous flow over the sphere, the problem is more complex due to the presence of boundary layers and the lack of an analytical solution. Therefore, the grid convergence analysis is conducted using three grid levels. See Ref.[5] for more details on convergence analysis.

3.1 Test-case 1: Eulerian flow in a hemisphere cylinder

The first model problem involves a Mach 10 flow past a hemispherical nose mounted on a circular cylinder. The free-stream is aligned with the body's axis of symmetry, resulting in an axisymmetric flow field but the simulation is conducted on the full 3D geometry, without assuming flow symmetry. The computational domain is an orthogonal parallelepiped with dimensions shown in Figure 5. In particular, Fig. 5.a shows the background mesh without the shock wave, also used in the S-C calculation, and Fig. 5.b shows the computational mesh used in the S-F calculation. The radius of the hemisphere and the height of the cylinder are taken as the reference length scale L. The cylinder axis is centered on the outflow plane, and the nose of the hemisphere is positioned at a distance L upstream of the inflow plane.

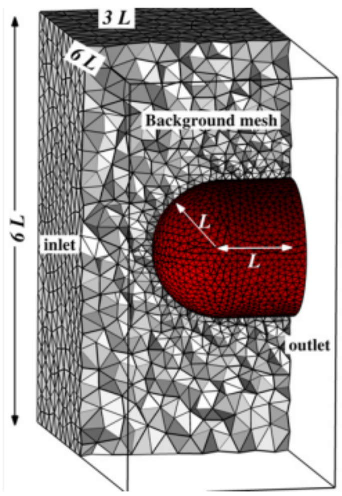

(a) Background mesh.

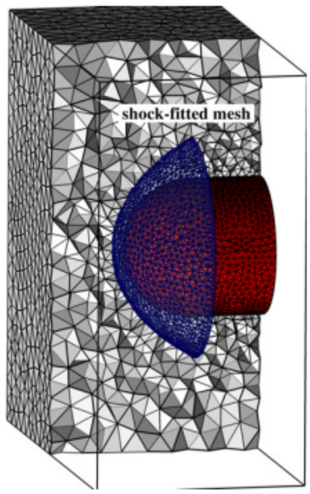

(b) Modified mesh.

Figure 5: Test-case 1: background and computational meshes

To assess the accuracy of the discretization, both global and local grid convergence analyses have been carried out using two nested background tetrahedral grids. The fine grid is generated by subdividing each element of the coarse grid into eight tetrahedra. Similarly, the surface triangulation of the bow shock is refined by splitting each triangle into four smaller elements. Table 1 provides the number of nodes and elements in the volume and surface meshes for each grid level.

DOI: 10.13009/EUCASS2025-227

Table 1: Test-case 1: mesh characteristics for both grid levels

Grid level	Volumetric background mesh		Shock-surface mesh	
	Grid points	Tetrahedra	Grid points	Triangles
0	13,520	72,022	2,053	4,032
1	108,164	576,177	8,212	16,128

Figure 6 compares the pressure distribution on the body surface obtained using S-C and S-F techniques. The left frame shows the S-C solution which clearly reveals an irregular pressure pattern and two pressure peaks distributed asymmetrically. This behavior is typical of S-C methods, where the shock is smeared over several grid cells, leading to reduced accuracy in shock localization as explained in the introduction. The right frame shows the solution obtained with the S-F method. It exhibits a well-defined symmetric and smooth pressure distribution centered around the stagnation point that suggest higher accuracy in the solution, compared to S-C.

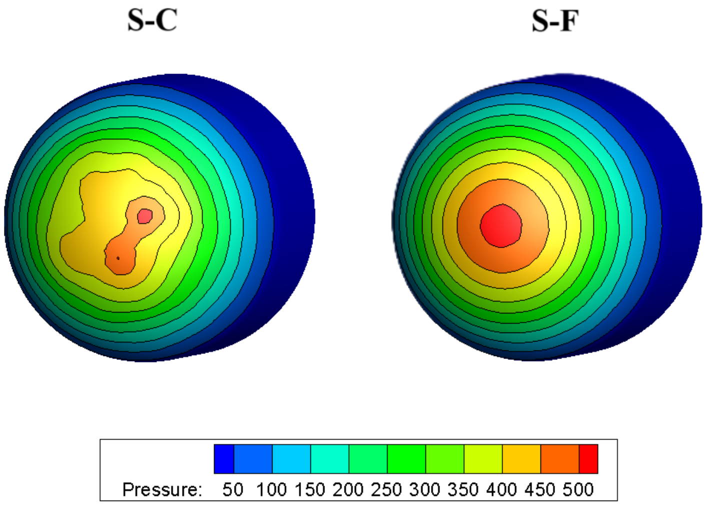

Figure 6: Test-case 1: surface pressure distribution. S-C versus S-F

The total temperature, which remains constant throughout the entire flowfield, is used to evaluate the global order-of-accuracy. A local estimate of the order-of-accuracy can also be obtained at the stagnation point, where the bow shock behaves as a normal shock along the stagnation streamline and the flow is brought to rest isentropically. The stagnation pressure can therefore be determined analytically, enabling a precise local assessment of the numerical accuracy. For the given free-stream conditions, total temperature and stagnation pressure equal 6237 K and 516.87 Pa, respectively.

The results of the grid convergence analyzes are reported in Tab. 2 and show that the measured order, $\tilde{n}$, is indeed close to the design (second) order for both the global and local analysis. This implies that both the coarse- and the fine-grid solutions are in the asymptotic range of convergence, that is, the terms in the discretization error of order higher than the design order are negligible.

Table 2: Test-case 1: global and local grid-convergence analyses based on total temperature and stagnation pressure

Grid level	$L_1(T^0_\infty - T^0_i)/T^0_\infty$	Computed p^h_{st}, Pa	p_{st}-p^h_{st}, Pa
0	1.023×10^{-6}	505.26	11.6
1	2.694×10^{-7}	513.567	3.03
$\tilde{n}$	1.926		1.937

DOI: 10.13009/EUCASS2025-227

3.2 Test-case 2: viscous laminar flow past a sphere

To assess the accuracy and robustness of the shock-fitting technique presented in Section 2.2, the classical benchmark proposed by Blottner[10] for hypersonic laminar flow over a sphere is considered. Free-stream values of the Mach ($M_\infty = 5$) and Reynolds ($Re_\infty = 1.88 \times 10^6$) numbers are representative of conditions where viscous effects and shock-boundary layer interactions play a significant role.
The computational domain, shown in Fig. 7, consists of a sphere with radius $R = 1$ m, enclosed by a spherical far-field boundary located at a distance $5R$ from the center of the sphere. Both the S-C and S-F approaches are applied to this case, and a detailed grid convergence analysis is performed. Due to the lack of analytically known quantities,

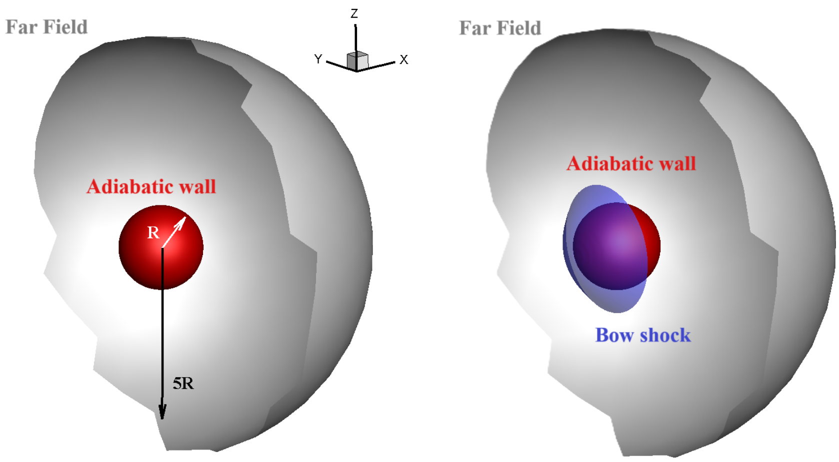

Figure 7: Computational domain for hypersonic viscous flow past a sphere

three levels of nested grids are employed, each obtained by systematically refining the background mesh and the shock surface triangulation, to evaluate the order of accuracy. The mesh characteristics of the three grid levels are reported in Tab. 3. It is worth emphasizing that the background mesh used in the S-C calculation and the computational mesh used in the S-F one only differ in the neighborhood of the fitted shock surface. Figure 8 presents a comparison of

Table 3: Test-case 2: mech characteristics of all three grid levels

Grid level	**Volumetric background mesh**		**Shock-surface mesh**	
	Grid points	Tetrahedra	Grid points	Triangles
0	37,108	216,171	1,215	2,336
1	296,864	1,729,368	4,860	9,344
2	2,374,912	13,834,944	19,440	37,376

the pressure fields obtained using the two methods: the S-C solution is computed on the finest grid level (Level 2), while the S-F solution uses the coarsest grid level (Level 0). The S-C solution exhibits a finite shock thickness that introduces spurious disturbances throughout the shock layer. In contrast, the S-F solution maintains a discontinuity of zero thickness, resulting in a clean shock layer free from unphysical oscillations. Moreover, the pressure gradients are well-resolved even on the coarse grid. This difference is also evident in the pressure iso-contour comparison shown in Fig. 8: the shock thickness remains visible in the S-C solution (red contours) despite the fine grid, whereas the S-F solution (black contours) clearly shows a zero-thickness shock, preserving accuracy even on the coarsest mesh.

The superior quality of the S-F solution is further confirmed by the dimensionless pressure distribution along the body surface, compared against Blottner's[2] numerical data. Figures 9 and 10 show comparisons for both the coarsest and finest grids, respectively. At grid level 0, the S-F solution (red line) aligns well with Blottner's data (black circles), whereas the S-C solution (blue line) deviates noticeably. On the finer grid (level 2), both methods match the reference data closely except near the stagnation region, where the S-F solution continues to show good agreement, while the S-C solution significantly diverges.

Finally, pointwise order estimates are given in Tab. 4 for the S-C simulations and in Tab. 5 for the S-F ones. R is the grid-convergence ratio defined as:

$$R = \epsilon_h(\mathbf{x}_i)/\epsilon_{rh}(\mathbf{x}_i) \tag{2}$$

DOI: 10.13009/EUCASS2025-227

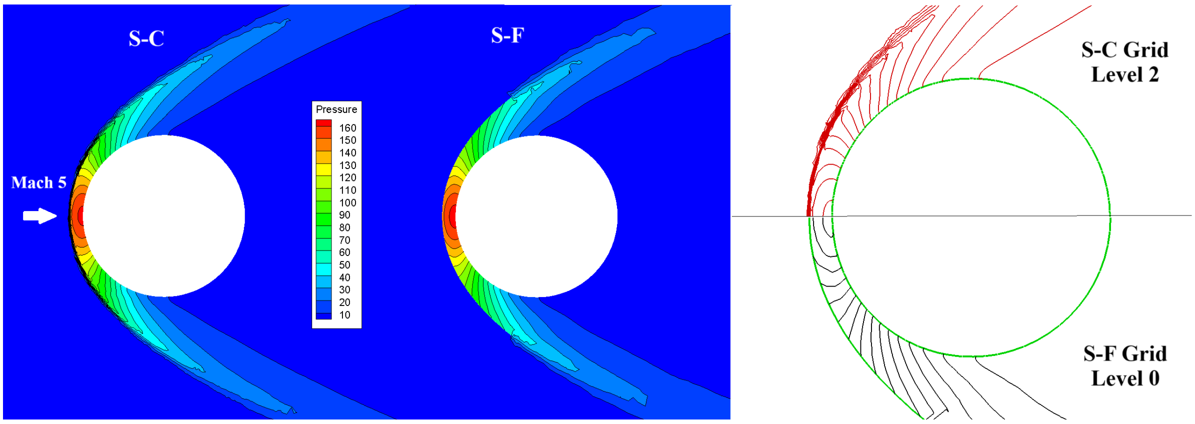

Figure 8: Test-case 2: pressure field and iso-contour lines computed using S-C and S-F

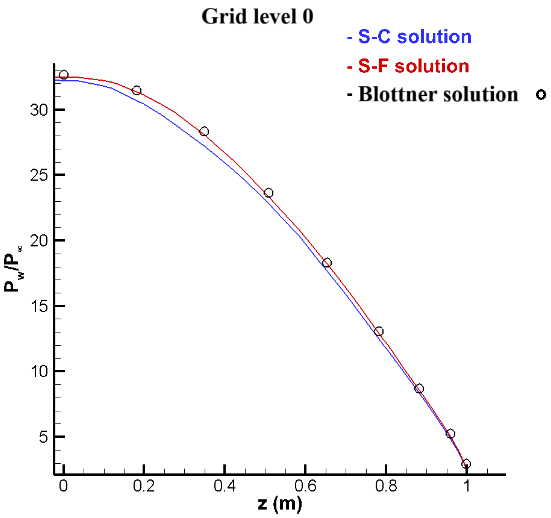

Figure 9: Comparison with Blottner[2] solution on the coarsest mesh

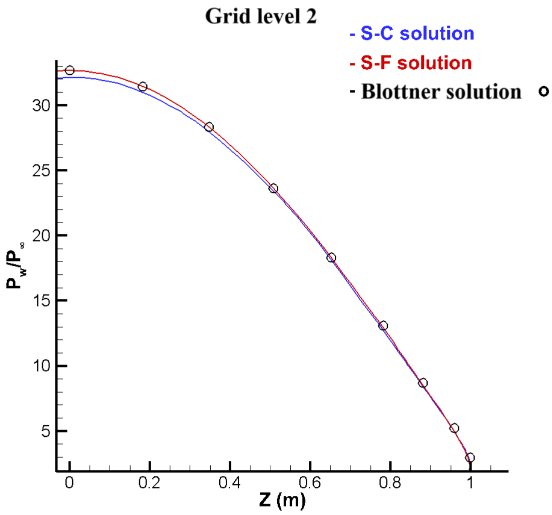

Figure 10: Comparison with Blottner[2] on the finest mesh

and can only be computed within each grid point of the coarser grid level rh, r being the grid-refinement ratio, here equal to 2. ϵ_h is the discretization error defined as the difference between the solution u_h to the discretized equations computed on a mesh of average spacing h and the exact solution u_0.
The grid-convergence ratio R allows to identify four different situations and classify the grid points according to the following criteria: monotone convergence ($0 \leq R \leq 1$); oscillatory convergence ($-1 < R < 0$); oscillatory divergence ($R < -1$); monotonic divergence: ($R > 1$). $\langle\tilde{n}\rangle$ is the mean observed order of accuracy, while $\sigma(\tilde{n})$ is the standard deviation.
Table 4 shows that in the S-C solution the number of monotonically converging grid points is around 50% with an observed order of accuracy $\tilde{n}$ close to design order 2 only in the case of the momentum. About 30% of grid points exhibit oscillatory convergence and about the 15% monotonic divergence. In the S-F solution the percentage of grid points in monotonic convergence is close to 90% with an observed order of accuracy close to the design order.
These results confirm the superior accuracy and convergence properties of the S-F approach. Indeed, while with the S-F method the observed order of accuracy is close to the design order, the S-C calculations exhibit first-order convergence, despite the scheme being formally second-order.

4. Fluid-structure Interaction (FSI) test-cases

Recently, the S-F alghoritm was extendend to deal with both steady and unsteady fluid-structure interaction. This FSI technique originates from the Shock-Fitting method described in Sec.2.2 and allows to describe the motion of a thin wall immersed in a fluid by treating it as a zero-thickness boundary of the fluid domain exposed to the spatially variable

DOI: 10.13009/EUCASS2025-227

Table 4: Test-case 2: point-wise analysis of the S-C solution

Variable	$0 < R < 1$	$\langle \tilde{n} \rangle$	$\sigma(\tilde{n})$	$-1 < R < 0$	$\langle n^* \rangle$	$R > 1$	$R < -1$
ρ	50.1%	1.682	2.531	30.6%	2.931	11.5%	7.9%
ρu	41.9%	1.100	2.607	28.2%	2.448	15.9%	14.0%
ρv	45.2%	2.098	4.303	29.3%	3.959	14.9%	10.6%
ρw	43.7%	2.073	4.341	30.1%	3.881	15.3%	10.9%
ρE	54.8%	0.847	2.476	15.3%	3.116	20.4%	9.4%

Table 5: Test-case 2: point-wise analysis of the S-F solution

Variable	$0 < R < 1$	$\langle \tilde{n} \rangle$	$\sigma(n)$	$-1 < R < 0$	$\langle n^* \rangle$	$R > 1$	$R < -1$
ρ	92.1%	2.632	1.437	4.83%	3.665	1.82%	1.25%
ρu	88.7%	2.320	1.617	6.92%	3.285	2.60%	1.79%
ρv	85.6%	2.498	1.783	8.81%	3.913	3.32%	2.28%
ρw	87.2%	2.373	1.742	7.83%	3.343	2.94%	2.02%
ρE	94.8%	2.051	1.504	3.18%	2.986	1.20%	0.82%

aerodynamic pressure produced by the external flow. While in the steady state case the structural and CFD models are weakly coupled, in the unsteady FSI simulation the geometrical compatibility conditions and the equilibrium conditions on the interface must be satisfied. For this reason, the Arbitrary Lagrangian-Eulerian (ALE) formulation available in the SU2[11] shock-capturing code was used to discretize the governing PDEs.
In the steady case implicit non-linear methods can be adopted to solve the structural displacement through load incrementation in which the total external load is divided into a series of smaller load steps, allowing the solver to progressively reach the final state.
In contrast, the unsteady case requires explicit nonlinear methods capable of ensuring solution stability and convergence under large deformation scenarios.
The FSI algorithm can be split into the following five main steps:

- Step 0 is identical to that described in Sec. 2.2: it allows to extract the initial position and shape of the shock wave.

- Step 1. The geometrical shape of the deformable wall geometry must also be inserted into the background mesh, in addition to the shock surface. Ghost points in this case will be formed by nodes too close to the shock wave plus those too close to or inside the moving deformable wall. The TetGen[23] mesh generator is then used to fill the cavities using a constrained Delaunay tetrahedralization, ensuring conformity to the triangulations of both the shock surface and the deformable solid surface. Figure 11 shows the surface triangulations of a bow shock and a parachute being inserted into the background mesh.

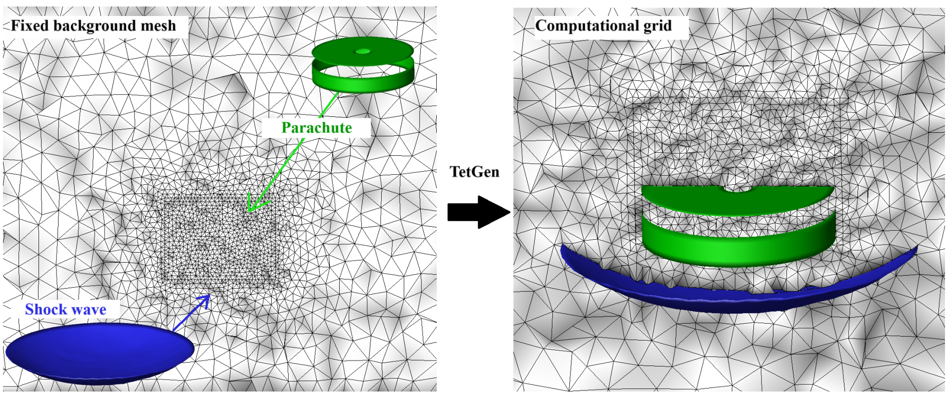

Figure 11: FSI algorithm: the computational mesh is obtained by inserting the shock surface and the deformable membrane of a parachute into the background mesh

- Step 2 is different depending on whether the FSI is steady or unsteady.

DOI: 10.13009/EUCASS2025-227

- **Steady simulation:** in the steady case the SU2 CFD code updates to time $t + \Delta t$ the nodal values at all gridpoints of the computational grid, which includes the shock-points on the upstream and downstream sides of the fitted shock and the gridpoints located on the wetted surfaces of the deformable membrane.
- **Unsteady simulation**: The positions of both the shock surface and the deformable wall at time $t + \Delta t$ are computed based on the flow solution at time t. The shock wave motion is determined by solving the Rankine-Hugoniot equations, while the deformation of the flexible wall is calculated using a structural solver that accounts for the differential pressure acting on the two sides of the surface. An example illustrating the displacement of both the shock wave and the parachute is shown in Fig. 12. The black lines indicate the initial positions of the discontinuities at $t = 0$, while the red lines depict their deformed shapes at $t + \Delta t$.

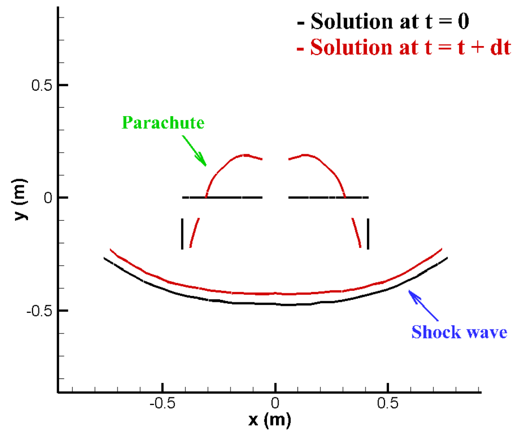

Figure 12: FSI algorithm: displacement of the shock wave and wall

- Step 3 is different depending on whether the FSI is steady or unsteady.
  - **Steady simulation:** the Rankine-Hugoniot equations provide the local speed of the gas-dynamics discontinuities and the new position of each shock node is computed according to Eq. (1). The displacement of the wall nodes is calculated using an implicit, non-linear structural solver. In particular, the deformation is determined by the pressure differential tacting on the two sides of the wall.
  - **Unsteady simulation:** The ALE methods of the SU2 code is used to solve the governing PDEs in the (smooth) regions of the flow-field bounded by the surfaces of discontinuity. The displacements of the shock wave and the parachute are supplied to SU2 which moves the surfaces in the considered time-step Δt.
- Step 4: All the ghost nodes of the background mesh, both around the shock and the moving membrane, must be interpolated for the same reason explained in Step 4 of Sec. 2.2.

5. FSI test-cases

In recent work, Orlandini et al.[19] proposed a test case that allows to compare the steady FSI simulation with an analytical solution. It consists of a thin membrane exposed to a supersonic flow on one of its sides, as shown in Fig. 13 where the free-stream flow conditions and the material properties of the membrane are also given. A similar setting is used here to validate the unsteady FSI technique. In both cases we assume small deformations of the membrane and the high-speed compressible flow is shock-less. The results of the FSI simulation are compared with the analytically computed displacement of a 2D membrane which is governed by the following non-linear o.d.e.:

$$\rho_m h \frac{\partial^2 w(x,t)}{\partial t^2} - T \frac{\partial^2 w(x,t)}{\partial x^2} = P(x,t). \tag{3}$$

In deriving Eq. (3) we neglect the deformation in the x-direction and we assume that the displacement, w, in the y-direction (or out-of-plane displacement) is sufficiently small that the tension T can be considered constant. Consistently

DOI: 10.13009/EUCASS2025-227

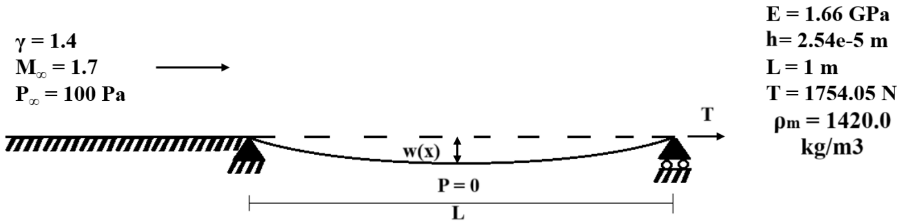

Figure 13: Test-cases 3 and 4: geometry of the membrane, material and flow properties

with the hypothesis of small deformations, the pressure distribution was considered independent of time, $P(x)$, and it is calculated using Ackeret's theory:

$$C_p = \frac{2}{\gamma M_\infty^2}\left(\frac{P(x)}{P_\infty} - 1\right) = \frac{2\theta}{\sqrt{M_\infty^2 - 1}}. \tag{4}$$

where M_∞ and P_∞ are the free-stream Mach number and static pressure, respectively, see Fig. 13.
Figure 15.a shows the computational domain used in the FSI simulation, whereas the structural model of the membrane is shown in Fig. 15.b. The computational mesh that fills the fluid domain (a box sized $L{\times}L/2{\times}L$) has the characteristics reported in Tab. 6.

Table 6: Test-cases 3 and 4: characteristics of the grids

Background		Membrane	
Grid Points	Tetrahedra	Grid Points	Triangles
39,333	229,031	1,681	3,200

In the structural model of the membrane of Fig. 15.b the nodes at $x = 0$ and $x = 1$ have all the degrees of freedom constrained, while the nodes at $z = \pm L/2$ are only allowed to translate along the y-axis to prevent displacements outside the CFD domain. In the steady case, the rotational degrees of freedom of all the other nodes are constrained in order to reproduce the membrane behavior by eliminating the bending stiffness and to overcome buckling problems.

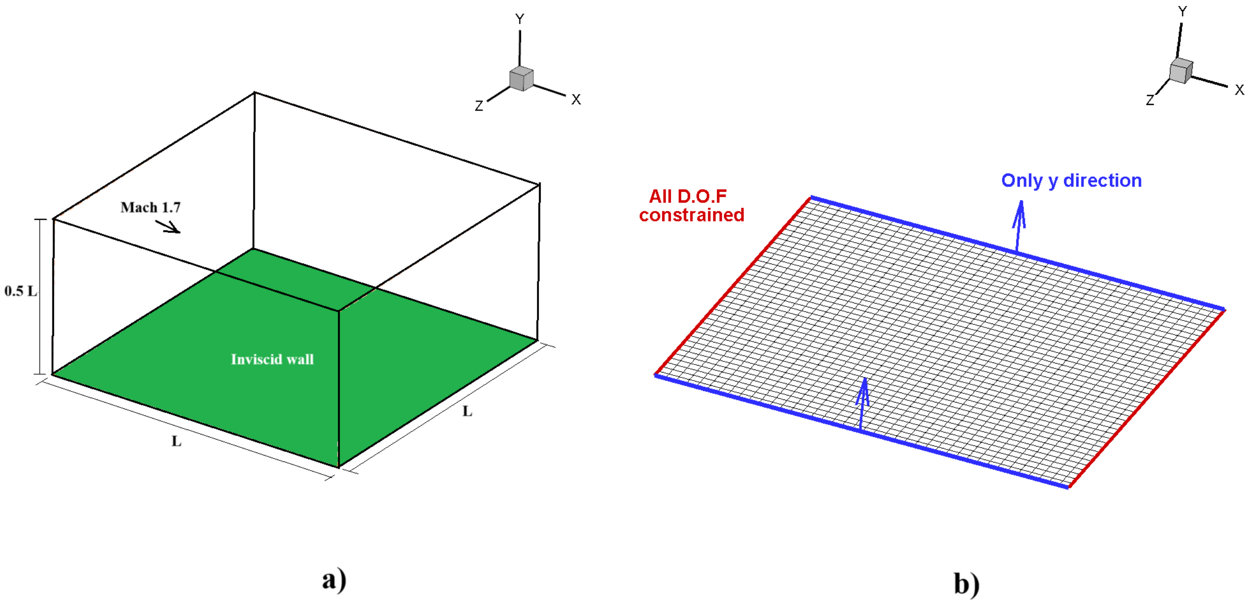

Figure 14: Test-cases 3 and 4: a) Computational domain; b) Structural model of the membrane

DOI: 10.13009/EUCASS2025-227

5.1 Test-case 3: Steady FSI solution on a deformable membrane

In the steady case, Eq. (3) reduces to the following linear o.d.e.:

$$\frac{d^2w(x)}{dx^2} = \frac{P(x)}{T} \tag{5}$$

Once we replace Eq. (4) in Eq. (5) and set the local slope of the membrane $\theta = \frac{dw}{dx}$, we obtain the following o.d.e.:

$$\begin{cases} \dfrac{d^2w}{dx^2} - \left(\dfrac{\gamma M_\infty^2}{\sqrt{M_\infty^2 - 1}}\dfrac{dw}{dx} + 1\right)\dfrac{P_\infty}{T} = 0 \\ w(0) = 0, \\ w(L) = 0. \end{cases} \tag{6}$$

When coupled with the boundary conditions stated above, the o.d.e. (6) has the following analytical solution:

$$\begin{aligned} w(x) &= \frac{Le^{abx}}{b(e^{ab}-1)} - \frac{L}{b(e^{ab}-1)} - \frac{x}{b}; \\ \text{with} \quad a &= \frac{P_\infty}{T}, \qquad b = \frac{\gamma M_\infty^2}{\sqrt{M_\infty^2 - 1}}. \end{aligned} \tag{7}$$

which will be used to validate the steady FSI steady technique.
Figure 15, which shows a zoom centered around $x = L/2$, reveals that the FSI simulation, shown using circular red markers, closely matches the analytical solution (7).

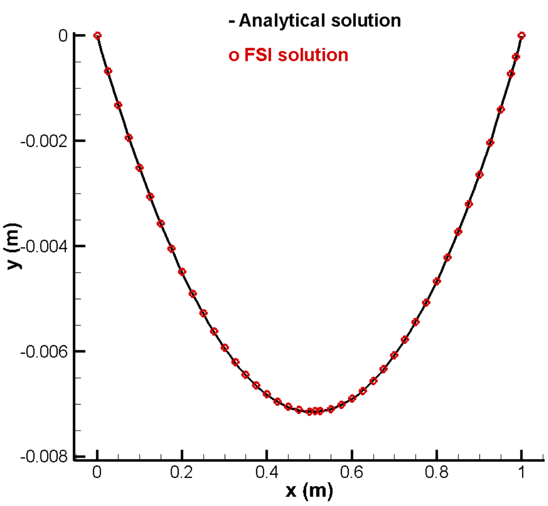

Figure 15: Test-cases 3: comparison between FSI and analytical solution in the steady case

5.2 Test-case 4: Unsteady FSI solution on a deformable membrane

In the unsteady case, an artificial damping term $c = 10$ kg m^{-2} s^{-1} was added to Eq. (2) to reduce the time required to reach the converged solution:

$$\rho_m h \frac{\partial^2 w(x,t)}{\partial t^2} + c\frac{\partial w(x,t)}{\partial t} - T\frac{\partial^2 w(x,t)}{\partial x^2} = P(x). \tag{8}$$

Since Eq. (8) cannot be solved analytically, a centered finite difference (FD) scheme was used instead. The pressure term $P(x)$, which is written in (8) using Ackeret's theory, can instead be replaced by a constant pressure distribution $P(x) = 100$ Pa to see the effect of the supersonic flow on the membrane. Figures 16 to 19 show four different snapshots of the solution at time $t = 0.004$ s, 0.009 s, 0.014 s and 0.5 s, the latter corresponding to the asymptotic, steady-state

DOI: 10.13009/EUCASS2025-227

solution. In each figure, composed of the overall solution and a zoom in the right panel, the black line represents the FD solution of (8) with $P(x)$ computed according to (4), the blue line corresponds to the solution obtained with $P(x) = 100$ Pa, while the red circular markers indicate the FSI solution. At each time step, the FD solution of Eq. (8), calculated using Ackeret's theory, is in good agreement with the FSI solution, showing instead a significant difference compared to the FD solution obtained assuming a constant pressure distribution. This discrepancy is due to the effect of the supersonic flow, which induces an asymmetric deformation not present in the case of uniform pressure. Figure (19) shows that the asymptotic solution of the unsteady problem coincides with that of the stationary problem, previously illustrated in Figure 15.

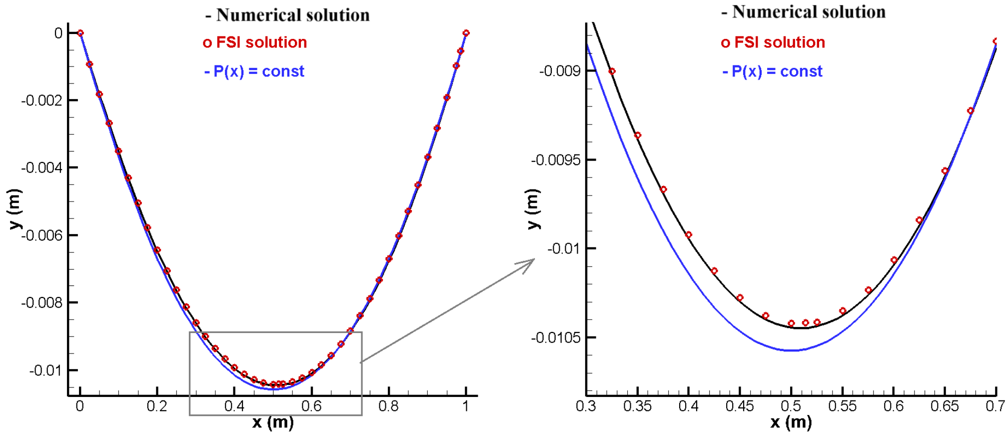

Figure 16: Test-cases 4: Comparison between the FSI and analytical solution at $t = 0.004$ s

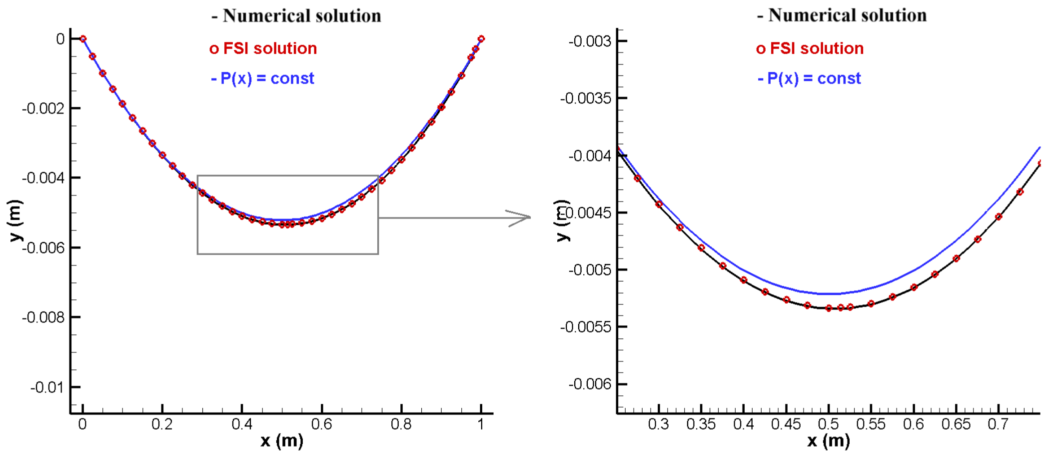

Figure 17: Test-cases 4: Comparison between the FSI and analytical solution at $t = 0.009$ s

6. Conclusions

A shock-fitting algorithm for unstructured meshes has been successfully integrated with the SU2 solver and validated through four test cases involving Eulerian and viscous hypersonic flows and FSI simulations. The method allows the representation of shock waves as real discontinuities within the fluid dynamic field by treating them as internal boundaries by the SU2 solver. Furthermore, the extension of this technique to fluid-structure interaction has allowed to consider deformable walls such as membranes just as zero-thickness discontinuities within the field just like in the case of shock waves. Shock-fitting simulations have demonstrated that, for high-speed flows with the presence of gasdynamic discontinuities, they offer superior resolution and accuracy compared to shock-capturing techniques,

DOI: 10.13009/EUCASS2025-227

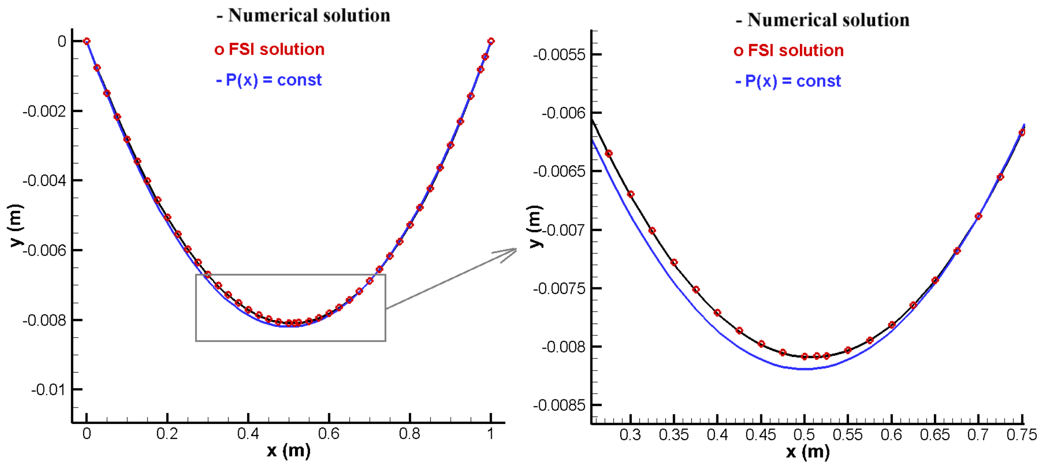

Figure 18: Test-cases 4: Comparison between the FSI and analytical solution at t = 0.014 s

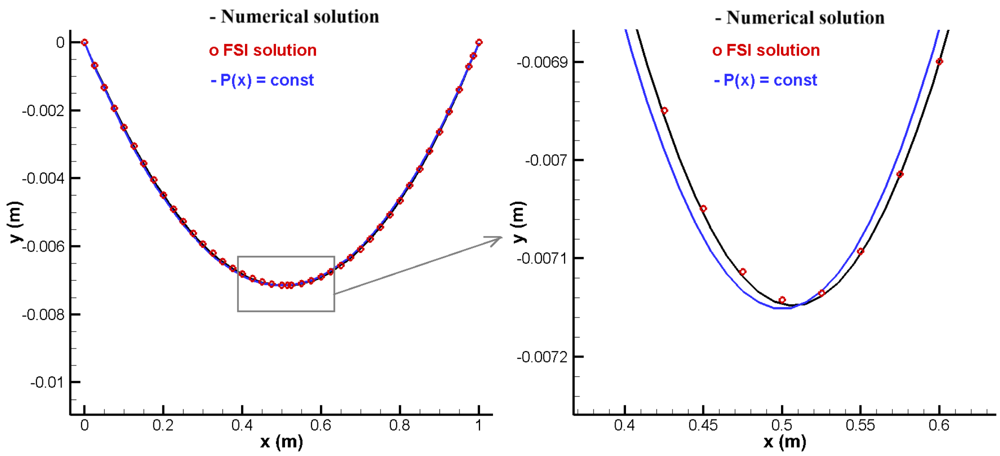

Figure 19: Test-cases 4: Comparison between the FSI and analytical solution at steady state

especially in stagnation regions. In small perturbations, it has been possible to demonstrate that the treatment of the deformable membrane through this technique, the reliability of the method even in fluid-structure coupled contexts. Indeed, for both the stationary and the non-stationary case, the analysis of the results shows us an excellent accuracy of the solution both for the comparison with the analytical and the numerical solution. In conclusion, the algorithm preserves a second-order accuracy in most of the domain and shows a significantly improved convergence behavior. These results suggest that shock-fitting represents a valid alternative to traditional approaches, especially for problems involving strong shocks. This approach, however, is only a first step as it must be extended to more complex problems such as in the presence of interactions between discontinuities in 3D that require more complex geometric challenges. In the FSI case, instead, it must be demonstrated that this technique can also work for large deformations, both in the absence and in the presence of discontinuities as can be the example of the inflation of a parachute.

References

[1] CAE Beta. Systems sa. *ANSA v12*, 1, 2015.

[2] Frederick G Blottner. Accurate Navier-Stokes results for the hypersonic flow over a spherical nosetip. *Journal of spacecraft and Rockets*, 27(2):113–122, 1990.

[3] A. Bonfiglioli. Validation of fluctuation splitting schemes for hypersonic calculations. Technical report, University of Michigan, 2004. Unpublished.

DOI: 10.13009/EUCASS2025-227

[4] Aldo Bonfiglioli, Bruno Carpentieri, and Masha Sosonkina. Eulfs: a parallel cfd code for the simulation of euler and navier-stokes problems on unstructured grids. In *International Workshop on Applied Parallel Computing*, pages 676–685. Springer, 2006.

[5] Aldo Bonfiglioli and Renato Paciorri. Convergence analysis of shock-capturing and shock-fitting solutions on unstructured grids. *AIAA journal*, 52(7):1404–1416, 2014.

[6] D. Bonhaus. *A higher order accurate finite element method for viscous compressible flows*. PhD thesis, Virginia Polytechnic Institute and State University, 1998.

[7] M. H. Carpenter and J. H. Casper. Accuracy of shock capturing in two spatial dimensions. *AIAA Journal*, 37(9):1072–1079, 1999.

[8] J. Casper and M. H. Carpenter. Computational considerations for the simulation of shock-induced sound. *SIAM Journal on Scientific Computing*, 19(3):813–828, 1998. Also NASA Langley RC Technical Memorandum 110222.

[9] G. V. Chandler, M. D. Barnhardt, T. W. Drayna, I. Nompelis, D. M. Peterson, and P. Subbareddy. Unstructured grid approaches for accurate aeroheating simulations. In *18th AIAA Computational Fluid Dynamics Conference*, Miami, FL, 2007. Paper 2007-3959.

[10] H. Deconinck, H. Paillère, R. Struijs, and P. Roe. Multidimensional upwind schemes based on fluctuation-splitting for systems of conservation laws. *Computer Methods in Applied Mechanics and Engineering*, 11(5/6):323–340, 1993.

[11] Thomas D Economon, Francisco Palacios, Sean R Copeland, Trent W Lukaczyk, and Juan J Alonso. Su2: An open-source suite for multiphysics simulation and design. *Aiaa Journal*, 54(3):828–846, 2016.

[12] H. W. Emmons. The numerical solution of compressible fluid flow problems. Technical Report NACA-TN 932, NASA, 1944.

[13] P. Gnoffo and J. A. White. Computational aerothermodynamic simulation issues on unstructured grids. In *AIAA Paper*, number 2004-2371, 2004.

[14] P. A. Gnoffo. Simulation of stagnation region heating in hypersonic flow on tetrahedral grids. In *18th AIAA Computational Fluid Dynamics Conference*, Miami, FL, 2007. Paper 2007-3960.

[15] P. A. Gnoffo. Multi-dimensional, inviscid flux reconstruction for simulation of hypersonic heating on tetrahedral grids. In *47th AIAA Aerospace Sciences Meeting*, Orlando, Florida, 2009. Paper 2009-599.

[16] M. Ivanov, A. Bonfiglioli, R. Paciorri, and F. Sabetta. Computation of weak steady shock reflections by means of an unstructured shock-fitting solver. *Shock Waves*, 20(4):271–284, 2010.

[17] G. Moretti. Computation of flows with shocks. *Annual Review of Fluid Mechanics*, 19:313–337, 1987.

[18] G. Moretti and M. A. Abbett. A time-dependent computational method for blunt body flows. In *AIAA Journal*, volume 4, pages 2136–2141, 1966.

[19] Valerio Orlandini, Renato Paciorri, Alessia Assonitis, and Aldo Bonfiglioli. Front-tracking technique for computing inflatable structures in hypersonic flows. *AIAA Journal*, pages 1–17, 2025.

[20] Valerio Orlandini, Renato Paciorri, Alessia Assonitis, Francesco Saltari, and Aldo Bonfiglioli. A fluid dynamics technique for modelling inflatable shield for re-entry or aerocapture missions. In *AIAA AVIATION 2023 Forum*, page 4425, 2023.

[21] R. Paciorri and A. Bonfiglioli. A shock-fitting technique for 2d unstructured grids. *Computers & Fluids*, 38(3):715–726, 2009.

[22] R. Paciorri and A. Bonfiglioli. Shock interaction computations on unstructured, two-dimensional grids using a shock-fitting technique. *Journal of Computational Physics*, 230(8):3155–3177, 2011.

[23] P. S. Rawat and X. Zhong. On high-order shock-fitting and front-tracking schemes for numerical simulation of shock-disturbance interactions. *Journal of Computational Physics*, 229(19):6744–6780, 2010.

DOI: 10.13009/EUCASS2025-227

[24] J. C. Robinet, J. Gressier, G. Casalis, and J. M. Moschetta. Shock wave instability and the carbuncle phenomenon: some intrinsic origin? *Journal of Fluid Mechanics*, 417:237–263, 2000.

[25] M. D. Salas. Shock-fitting method for complicated two-dimensional supersonic flows. In *AIAA Journal*, volume 14, pages 583–588, 1976.

[26] Hang Si. A quality tetrahedral mesh generator and three-dimensional delaunay triangulator. *Weierstrass Institute for Applied Analysis and Stochastic, Berlin, Germany*, 81:12, 2006.

[27] Venkat Venkatakrishnan. Convergence to steady state solutions of the euler equations on unstructured grids with limiters. *Journal of computational physics*, 118(1):120–130, 1995.